

# Oxygen Reduction Reaction Catalyzed by Metal-Nitrogen–Carbon Hybrids Derived from Metal-Organic Frameworks: Optimized Performance by Zinc Porogen

John Diniz<sup>1</sup>, Eaindar Soe<sup>1</sup>, Jia En Lu<sup>1</sup>, Jesse Hauser<sup>1</sup>, Ahmad Shaabani<sup>2</sup>, Scott R. J. Oliver<sup>1,\*</sup>, and Shaowei Chen<sup>1,\*</sup>

<sup>1</sup>Department of Chemistry and Biochemistry, University of California, Santa Cruz, CA 95064, United States

<sup>2</sup>Department of Chemistry, Shahid Beheshti University, Tehran, 19834, Iran

## ABSTRACT

Carbon-based nanocomposites have been attracting extensive attention as viable candidates to replace platinum in the electrocatalytic reduction of oxygen, a critical process at fuel cell cathode. One unique system is carbon-supported iron carbide (Fe<sub>3</sub>C/C) catalysts derived pyrolytically from metal organic frameworks (MOFs). Herein, a series of Fe<sub>3</sub>C/C nanocomposites were produced by pyrolysis at a controlled temperature of FeMOF-NH<sub>2</sub> with a systemic variation of the iron and zinc compositions in the MOF precursor. Scanning/transmission electron microscopy, X-ray photoelectron spectroscopy, and X-ray diffraction measurements were carried out to examine the morphologies, structures, and elemental composition of the nanocomposites, while nitrogen adsorption/desorption and Raman studies were carried out to evaluate the surface area and porosity. The results showed that an optimal zinc to iron feeding ratio was required to prepare a catalyst with a preferential pore size distribution. In electrochemical measurements, the sample derived from 20% zinc replacement in the FeMOF-NH<sub>2</sub> precursor exhibited the best activity in the electrocatalytic reduction of oxygen in alkaline electrolytes among the series, with the most positive onset potential and highest limiting current, which coincided with the highest surface area and porosity. The results suggest that deliberate structural engineering is critical in manipulating and optimizing the electrocatalytic activity of metal, nitrogen-codoped carbon nanocomposites.

**KEYWORDS:** Metal Organic Framework, Porogen, Iron Carbide, Nanocomposite, Oxygen Reduction Reaction.

## 1. INTRODUCTION

Fuel cells represent an important technology in the pursuit of green energy and reduced pollution to the environment, where electricity is generated when fuel molecules are oxidized at the anode and oxygen is reduced at the cathode.<sup>26</sup> In polymer electrolyte membrane fuel cells (PEMFC), while the oxygen reduction reaction (ORR) is thermodynamically favorable, the poor kinetics necessitate the application of an effective electrocatalyst. Therefore, design and engineering of high-performance ORR electrocatalysts is vital in the advancement of PEMFC technology. In current practice, graphitic carbon-supported platinum nanoparticles (Pt/C) are utilized as the catalyst of choice, but the high cost and low natural abundance of platinum prevents the technology from being viable. Therefore, catalysts free

of precious metals have been attracting particular attention. Within this context, porous carbon doped with select metal and nonmetal elements have been observed to display obvious ORR activity, where the performance may even rival that of Pt/C,<sup>15,21</sup> owing to their large surface area, high chemical stability, and excellent electrical conductivity.<sup>8,29</sup>

One of the advancements is the development of nanocarbon-supported iron carbide catalysts.<sup>33,38</sup> For instance, a nanocomposite based on iron carbide nanoparticles encapsulated within a hollow carbon sphere (Fe<sub>3</sub>C–Fe,N/C) has been synthesized from iron (III) chloride and melamine using a triblock copolymer as the structural scaffold and exhibited a high specific area of 879.5 m<sup>2</sup> g<sup>-1</sup> and apparent electrocatalytic activity towards ORR.<sup>32</sup> Activation in an inert atmosphere of the similar transition metal-polymer composite through pyrolysis can further improve the catalytic activity. Mixtures of low-cost transition metal salts and nitrogen precursors for the macrocycles

\*Authors to whom correspondence should be addressed.

Emails: soliver@ucsc.edu, shaowei@ucsc.edu

Received: 4 December 2019

Accepted: 22 February 2020

can also be used to prepare ORR catalysts.<sup>17</sup> Fe<sub>3</sub>C/C catalysts have also been prepared by pyrolysis of polymers such as poly(1,8-diaminonaphthalene), polyvinylpyrrolidone, and polyacrylamide.<sup>7,9,20,41</sup> Fe<sub>3</sub>C/C catalysts derived from organic materials coordinating with iron have also shown good ORR activity.<sup>10,16,45</sup> It is argued that iron carbide can affect the work function of carbon and facilitate oxygen adsorption.<sup>38</sup>

One effective strategy to prepare such carbon-based ORR catalysts is controlled pyrolysis of metal-organic frameworks (MOFs), where metal and nonmetal elements from the MOF precursors are incorporated into the carbon skeletons.<sup>18</sup> Thus, a catalyst can be designed from the bottom up to take advantage of the ready manipulation of the MOF composition and structure. The first MOF derived ORR catalyst was prepared by pyrolyzing cobalt imidazolate frameworks (active Co-IM) at high temperatures, and significant progress has been achieved ever since.<sup>25</sup> Among these, iron and carbon catalysts for ORR have been prepared from select MOFs.<sup>18</sup> As catalysts derived from zinc-based MOFs have a wider distribution of pore sizes, iron-based MOFs such as MIL-88B-NH<sub>3</sub> have been used to develop carbonized nanoparticles through pyrolysis to reduce pore size distribution and produce metal active sites for high-performance ORR electrocatalysis.<sup>49</sup> For instance, catalysts have been developed from the pyrolysis of an iron-doped ZIF-8, a MOF containing both zinc and iron coordination, with a uniform iron distribution in a nitrogen-doped carbon matrix, and exhibited apparent ORR activity and sufficient stability in 0.1 M HClO<sub>4</sub>.<sup>37</sup> Among these, catalysts made up of iron carbide particles supported by carbon are of particular interest.<sup>28</sup> In fact, ZIF-8 has been utilized as a template with pyrrole and iron (III) chloride to be heated at elevated temperatures to form iron carbide nanoparticles encapsulated in bamboo-like nitrogen doped nanotubes as ORR catalysts, where the ORR activity was ascribed to the FeN<sub>x</sub> moieties and the carbon-encapsulated iron carbide, with a low yield of hydrogen peroxide in both 0.5 M H<sub>2</sub>SO<sub>4</sub> and 0.1 M KOH.<sup>1</sup> In fact, catalysts with iron carbide active sites have been developed in the last several years.<sup>23,24,27,31,35,44,47</sup>

To control the porosity of the resulting catalysts, carbon foams with hierarchical pores that consist of micro, meso and macropores are developed by solvent-assisted linker exchange before pyrolysis. For instance, when ZIF-8 was immersed in a 1H-1,2,3-triazole and methanol solution for three days, the resulting MOF yielded a catalyst that displayed an onset potential ( $E_{\text{onset}}$ ) of  $-0.030$  V versus Ag/AgCl in alkaline media and  $+0.570$  V in acidic media, much better than that without exchange.<sup>48</sup> In another study,<sup>14</sup> a B and N codoped porous carbon polyhedral catalyst was synthesized by treating pyrolyzed (800 °C) ZIF-11 with phenylboronic acid, sonication and drying before a second pyrolysis at 1000 °C, which showed the disappearance of micropores and a concurrent

increase in mesoporosity during the boron doping process. Another approach taken is a dual template method where a monolith of ordered polystyrene spheres and solution of Pluronic F127 and iron (II and III) chloride is used to template the production of macropores and mesopores, respectively, in a hierarchical structure of a porous spherical network of carbon.<sup>36</sup> These structures were adsorbed onto the graphene surface to increase electrical conductivity and uplift ORR activity. Single site FeN<sub>x</sub> moieties were distributed between the graphene sheet and the porous structures, resulting in a catalyst that was more active than commercial Pt/C in 0.1 M KOH. Porous carbon has also been derived from pyrolysis of biomass (e.g., powdered cattle bones) with single iron atom sites promoted by a combination of iron (II) phthalocyanine and unsubstituted phthalocyanine resulting in a catalyst with similar onset potential and activity and enhanced stability, in comparison to commercial Pt/C.<sup>46</sup>

Herein, a series of iron carbide@N-doped graphitic nanoparticles (FeNC) were pyrolytically derived from FeMOF-NH<sub>2</sub> with the same organic linkers but at different feeding ratios of the zinc and iron metal centers. The catalysts exhibited a similar prism geometry to the precursory MOFs, but with a porous graphitic surface. The evaporation of zinc compounds during pyrolysis increased the pore size and surface area, while graphitization of the MOF and encapsulation of Fe<sub>3</sub>C nanoparticles occurred. An optimal zinc to iron feeding ratio in the MOF precursor was identified that resulted in a nanocarbon material with a desirable distribution of mesopores, which facilitated the accessibility of the catalytic active sites and mass transfer of reaction intermediates and electrolyte ions, hence leading to enhanced ORR performance.

## 2. EXPERIMENTAL DETAILS

### 2.1. Chemicals

Iron (III) chloride hexahydrate (FeCl<sub>3</sub> · 6H<sub>2</sub>O, 99.9%, Fisher Scientific), 2-aminoterephthalic acid (99%, Acros Organic), zinc chloride (ZnCl<sub>2</sub>, 98%, Tokyo Chemical Industry), hydrochloric acid (HCl, 37%, Sigma-Aldrich), Pt/C (20 wt.%, Alfa Aesar), potassium hydroxide (KOH, Fisher Chemicals), and Nafion®117 solution (~5% in a mixture of lower aliphatic alcohols and water, Aldrich Chemistry) were all used as received. Water was purified with a Barnstead Nanopure Water System (resistivity 18.3 MΩ cm).

### 2.2. Sample Preparation

The MOF precursors were synthesized by adopting a previously reported method.<sup>4</sup> In brief, 2-aminoterephthalic acid and FeCl<sub>3</sub> were mixed at a mass ratio of 1:3 by dissolving each into 5 mL of ultra pure water and then combining them into a 15 mL Teflon-lined autoclave and heated for 24 h at 110 °C. The sample was then filtered, washed with water,

and dried at ambient temperature to produce an orange-red solid. Two additional MOFs were prepared in the same manner except that a (mass) fraction of the iron (III) chloride hexahydrate was replaced with zinc chloride. The resulting samples were referred to FeMOF-NH<sub>2</sub>-*n* (*n* = 1, 2 and 3, corresponding to 0, 20 and 30% Zn replacement in the MOF). To synthesize the ORR catalysts, the MOFs obtained above were ground by mortar and pestle and heated in a tube furnace (MTI GSL-1100X) under ultrahigh purity nitrogen at the flow rate of 200 cm<sup>3</sup> · min<sup>-1</sup> at 900 °C for one hour, producing a black flaky powder denoted as FeNC-*n*.

### 2.3. Characterization

X-ray diffraction (XRD) patterns were collected with a Rigaku SmartLab diffractometer with Cu K<sub>α</sub> ( $\lambda = 1.54 \text{ \AA}$ ) radiation operated at 40 kV and 44 mA. The XRD patterns of the MOF precursors were recorded from  $2\theta = 2^\circ$  to  $35^\circ$  at the scan rate of  $3^\circ \text{ min}^{-1}$  with the step size of  $0.01^\circ$ , and diffraction data of the ORR catalysts were collected from  $2\theta = 10^\circ$  to  $80^\circ$  at the scan rate of  $0.33^\circ \text{ min}^{-1}$  with the step size of  $0.01^\circ$ . Scanning electron microscopy (SEM) images were taken with a FEI Quanta 3D field emission microscope. Transmission electron microscopy (TEM) and elemental mapping studies were performed with a Philips CM300 scope at 300 kV. X-ray photoelectron spectra (XPS) were acquired with a PHI X-tool Instrument. Brunauer-Emmett-Teller (BET) surface area and pore volume analysis was carried out with a micropore size and chemisorption analyzer (Quantachrom Autosorb). Raman spectroscopic studies were carried out with a Delta NU Raman 532 nm spectrometer.

### 2.4. Electrochemistry

Voltammetric measurements were conducted with a CHI 710C electrochemical workstation using a rotating gold ring-glassy carbon disk electrode (RRDE), a Ag/AgCl reference electrode, and a graphite rod counter electrode. The Ag/AgCl reference was calibrated against a reversible hydrogen electrode (RHE); and the potentials in

the present work were reported with respect to this RHE. To prepare a catalyst ink, 1.0 mg of the FeNC catalysts prepared above was dispersed in 1 mL of ethanol along with 10  $\mu\text{L}$  of Nafion by ultrasonication. 10  $\mu\text{L}$  of the ink was dropcast onto the glassy carbon electrode and allowed to dry in air. Then 3  $\mu\text{L}$  of a Nafion:ethanol (v:v 1:4) solution was cast on top and allowed to dry. The corresponding catalyst loading was estimated to be  $0.0407 \text{ mg} \cdot \text{cm}^{-2}$  on the disk electrode surface.

## 3. RESULTS AND DISCUSSION

To investigate the effect of zinc content on the morphology and catalytic performances of the catalysts, three FeMOF-NH<sub>2</sub>-*n* MOFs were prepared at different zinc feed ratios. Figure 1 illustrates the synthesis from organic and salt precursors to the FeNC catalysts. From SEM measurements (Figs. 1(b, c)), the overall morphology of the FeNC-2 sample can be seen to resemble that of the FeMOF-NH<sub>2</sub>-2 precursor. Additionally, the FeNC-2 catalyst consists of micrometer-scale porous carbon whose surface contains nanoparticles with a diameter of ca. 500 nm. Whereas the overall geometry of short prisms with pointed ends in the FeMOF-NH<sub>2</sub> is preserved during pyrolysis, the surface of FeNC-2 is more textured with folds along the surface and smaller particles below the surface. From Figure 1(c), it can be seen that FeNC-2 exhibits geometric carbon structures with particles embedded in the surface. This can be further manifested in TEM measurements (Figs. 2(a, b)) which clearly show that dense particles were encapsulated in a carbon matrix. EDX elemental mapping (Fig. 3) reveals that the nanoparticles under the surface of FeNC-2 are of an iron compound and confirms the surrounding material as graphitic carbon with oxygen and nitrogen throughout. Indeed, from HRTEM measurements (Figs. 2(c, d)), the sample can be seen to exhibit well-defined lattice fringes with the interplanar spacing varying from 3.10  $\text{\AA}$  to 3.95  $\text{\AA}$ . This is attributed to graphitic (002) carbon where the *d* spacing expands somewhat, as compared to that of pristine graphite, because of thermal treatment at elevated temperatures.<sup>2</sup> The 6.28  $\text{\AA}$  Moiré

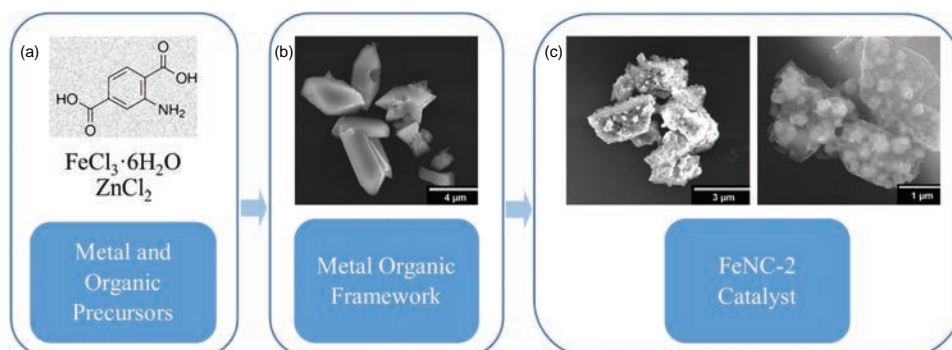


**Fig. 1.** Schematic diagram illustrating the synthesis of FeNC nanocomposites: (a) Metal salt and organic precursors used to synthesize FeMOF-NH<sub>2</sub>; (b) SEM image of FeMOF-NH<sub>2</sub>-2 before pyrolysis; (c) SEM image of the final product after pyrolysis, FeNC-2.

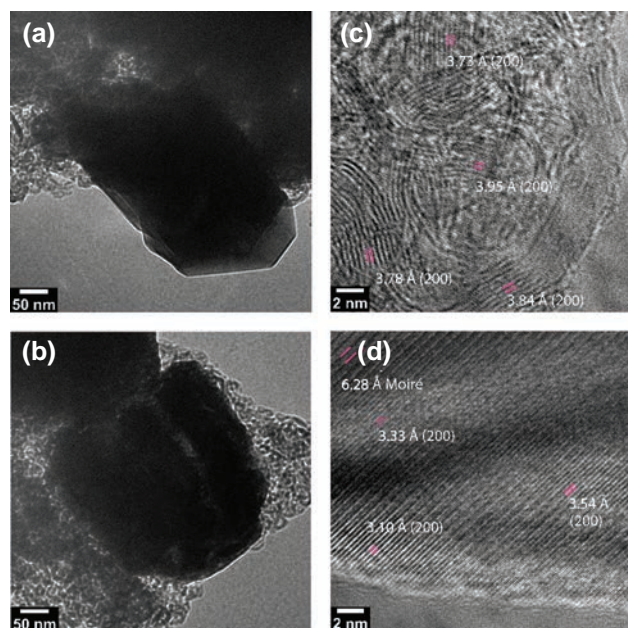


**Fig. 2.** (a, b) TEM and (c, d) HRTEM images of FeCN-2 showcasing the well-defined lattice fringes.

fringe is due to interference from overlapping interlayer spacings.<sup>34</sup> Taken together, results from the SEM and TEM studies show that pyrolysis of the MOF precursors yielded iron and nitrogen doped carbon which contained iron nanoparticles encapsulated within a graphitic shell.

All as-synthesized FeMOF-NH<sub>2</sub>-*n* MOFs show the characteristic XRD patterns corresponding to those of Fe-MIL-53-NH<sub>2</sub> at  $2\theta = 6.86^\circ, 8.86^\circ, 17.1^\circ$  and  $26.5^\circ$ , as reported previously.<sup>4</sup> Note that the XRD patterns remained unchanged as the feed ratio of zinc increased, suggesting the crystalline characteristics of the MOFs were not affected by the incorporation of zinc. Figure 4 depicts the corresponding XRD patterns of the FeNC samples obtained by pyrolysis of the FeMOF-NH<sub>2</sub>-*n* MOFs. All samples can be seen to show a sharp diffraction peak at

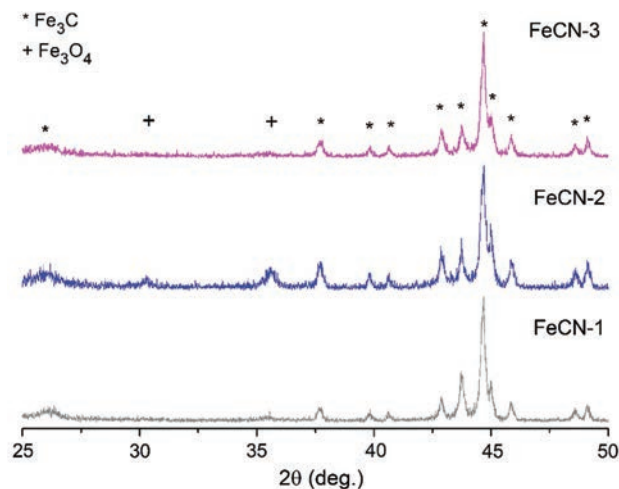


**Fig. 4.** PXRD patterns of the FeNC catalysts.

$26.1^\circ$ , due to the (002) plane of graphitic carbon, and the peaks at  $43.8^\circ, 44.7^\circ$  and  $50.8^\circ$  could be assigned to cementite (Fe<sub>3</sub>C, G23753) and magnetite (Fe<sub>3</sub>O<sub>4</sub>, AMCS0002400).<sup>13,39</sup> These results indicated that graphitic carbon, Fe<sub>3</sub>C, and Fe<sub>3</sub>O<sub>4</sub> were formed in the FeNC nanocomposites. Using the Scherrer equation,  $\tau = K\lambda/\beta \cos\theta$ , the mean size of the crystallites was estimated to be about 39 nm for the iron carbide assuming a *K* constant of 0.9. Since this is much smaller than the 500 nm particles seen in TEM measurements (Fig. 2), the result indicates that the particles most likely contained a polycrystalline structure.

The elemental composition and valence state of the samples were then examined by XPS measurements. In the survey profiles, the C, N, Fe and O elements can all be clearly defined in the FeNC series, suggesting that indeed Fe and N were successfully doped into the carbon skeletons. Figure 5(a) shows the high-resolution spectra of the C 1s electrons. For the FeNC-1 and FeNC-2 samples, deconvolution yields a peak at 283 eV due to carbon in Fe<sub>3</sub>C, another one at 284 eV to *sp*<sup>2</sup> C, and a third one at

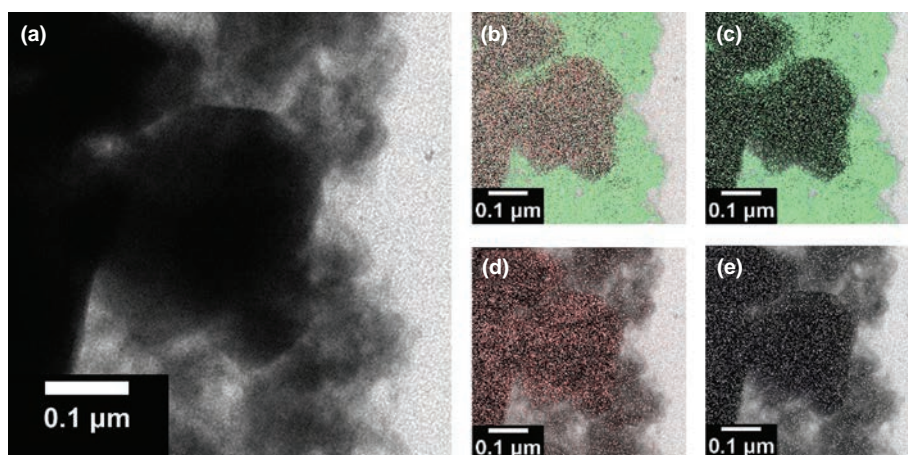


**Fig. 3.** (a) TEM image of FeCN-2, with the corresponding elemental maps of (b) combined elements, (c) carbon, (d) iron, and (e) nitrogen.

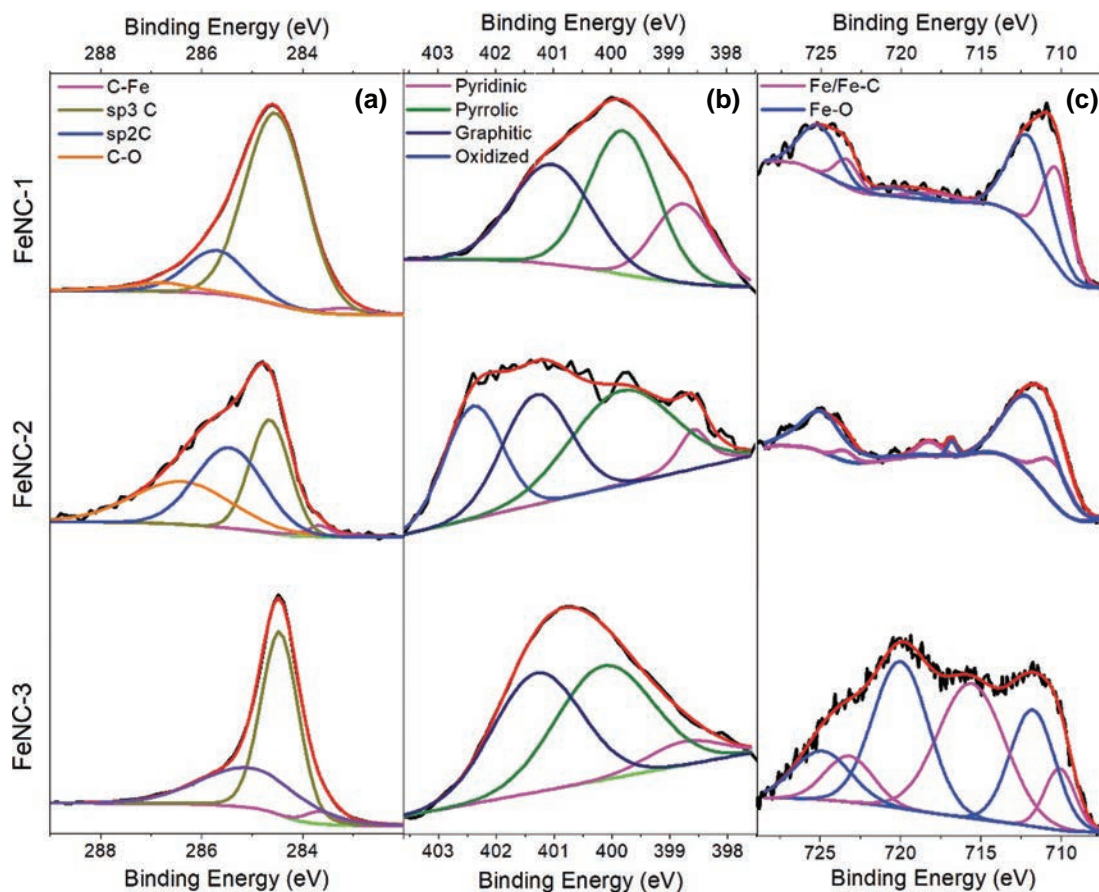


**Fig. 5.** High-resolution XPS spectra of the (a) C 1s, (b) N 1s, and (c) Fe 2p electrons in the FeNC nanocomposites. Black curves are raw data, whereas colored ones are deconvolution fits, as specified in the legends.

285 eV to  $sp^3$  C, with the peak at 286 eV indicative of C–O.<sup>3, 6, 11, 12, 22</sup> For FeNC-3, however, this C=O carbon cannot be resolved, and instead there is an additional peak of carbonate.<sup>3, 5</sup>

The N 1s scans are shown in Figure 5(b). All three FeNC samples can be seen to include peaks at 399, 400, and 401 eV, which are assigned to pyridinic N, pyrrolic N, and graphitic N, respectively, confirming successful doping of nitrogen into the carbon matrices.<sup>22</sup> From Table I, one can see that nitrogen accounted for 0.58 at% for FeNC-1, 1.52 at% for FeNC-2 and 0.56 at% for FeNC-3. That is, FeNC-2 contained the highest concentration of N dopants among the series.

The corresponding Fe 2p spectra are depicted in Figure 5(c). One can see that the binding energy of

Fe 2p in Fe–C decreased in the order of FeNC-1 (710.4 eV)  $\approx$  FeNC-2 (710.4 eV) > FeNC-3 (710.2 eV), whereas the corresponding C 1s binding energy increased in the order of FeNC-1 (283.2 eV) < FeNC-2 (283.6 eV) < FeNC-3 (283.8 eV), indicative of increasing carbon to iron charge transfer from FeNC-1 to FeNC-2 and to FeNC-3.<sup>19, 40, 43</sup> In addition, FeNC-2 can be seen to have the least amount of iron at 0.80 at%, less than half of those of FeNC-1 and FeNC-3, but have the greatest nitrogen to iron ratio. In fact, FeNC-2 has the highest concentration of Fe–C bonds, which is conducive to ORR electrocatalysis.

The porosity and surface area of the samples were then examined by nitrogen adsorption–desorption measurements. FeNC-2 exhibited a type IV isotherm with an H3 hysteresis loop, typical of capillary condensation in mesopores in the form of aggregates of plate like particles giving rise to slit shaped pores.<sup>30</sup> The FeMOF-NH<sub>2</sub>-2 precursor showed a surface area of 261 m<sup>2</sup> · g<sup>-1</sup> by the density functional theory (DFT) method and 433 m<sup>2</sup> · g<sup>-1</sup> from multi-point BET, a pore volume of 0.415 cm<sup>3</sup> · g<sup>-1</sup>, and a half pore width of 2.18 nm. After pyrolysis at 900 °C for 1 h, the resulting catalyst (FeNC-2) displayed a specific surface area of 746.0 m<sup>2</sup> · g<sup>-1</sup> by the DFT method and

**Table I.** Elemental compositions by XPS measurements.

Sample	Carbon (at%)	Iron (at%)	Nitrogen (at%)	Oxygen (at%)
FeNC-1	79.7	2.64	0.58	17.1
FeNC-2	82.5	0.80	1.52	15.2
FeNC-3	88.0	1.60	0.56	9.85

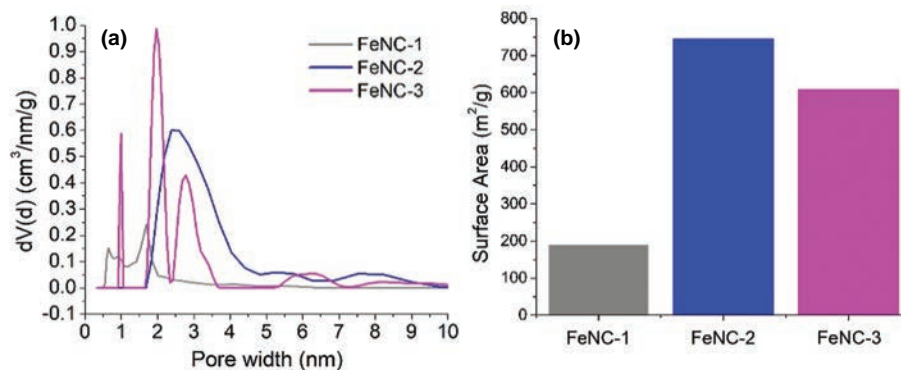


**Fig. 6.** (a) BJH plots of the FeNC series. (b) Surface area obtained from the DFT method.

771  $\text{m}^2 \cdot \text{g}^{-1}$  from multi-point BET (Fig. 6(b)), a pore volume of  $1.267 \text{ cm}^3 \cdot \text{g}^{-1}$ , and a half pore width of 2.38 nm, suggesting drastic enhancement of the porosity. This is largely due to the low boiling point (volatility) of the zinc compounds in FeMOF-NH<sub>2</sub>, which acted as an activating agent by evaporating out of the structure during pyrolysis creating pores in the carbon skeletons.

For comparison, from BET measurements (Fig. 6(b)), FeNC-1 displayed a surface area of  $189.2 \text{ m}^2 \cdot \text{g}^{-1}$  by the DFT method and  $213.5 \text{ m}^2 \cdot \text{g}^{-1}$  from multi-point BET, a half pore width of 1.692 nm, and a pore volume of  $0.242 \text{ cm}^3 \cdot \text{g}^{-1}$ . FeNC-3 has a surface area of  $607.7 \text{ m}^2 \cdot \text{g}^{-1}$  by the DFT method and  $557.4 \text{ m}^2 \cdot \text{g}^{-1}$  from multi-point BET, a half pore width of 1.970 nm, and a pore volume of  $0.773 \text{ cm}^3 \cdot \text{g}^{-1}$ . Interestingly, FeNC-2 exhibited a greater surface area and pore volume than FeNC-3, whereas FeNC-1 has the smallest surface area and pore volume. During pyrolysis, zinc acted as the activating agent in the FeMOF-NH<sub>2</sub> precursors creating porosity in FeNC. As FeMOF-NH<sub>2</sub>-1 lacks zinc, this activation was not present during pyrolysis resulting in the smallest surface area, pore width and volume. This is in good agreement with both FeNC-2 and FeNC-3 having a substantially greater surface area and pore volume than FeNC-1, with FeNC-2 having the highest surface area, pore volume and half-pore width overall. In addition, the fact that FeNC-3 displayed a smaller surface area and pores than FeNC-2 suggests that an optimal amount of zinc in the feeding ratio can be identified for the creation of larger pores.

To further understand porosity of these samples, the pore size distributions can be observed in the Barrett-Joyner-Halenda (BJH) plots in Figure 6(a). The distribution of FeNC-2 peaks broadly at 2.38 nm with no features below 2 nm. There is negligible presence of micropores in FeNC-2. The broad peak indicates a wide and continuous distribution of pore sizes. The distribution of FeNC-3 lacks this peak and instead peaks at 1.00 nm, 1.97 nm (both micropores) and 2.78 nm. These three narrow peaks indicate a trimodal distribution of pore sizes that are non-continuous. FeNC-1 has smaller broad peaks at 0.65 nm and 1.85 nm and thus only contains micropores. From the

peak intensities, FeNC-1 appears as the least porous sample. The different pore size distributions for each of the samples indicates that the zinc feeding ratio affects not just the surface area, pore volumes and mode pore widths, but the distribution in width, intensity and width centers. An optimal zinc feeding ratio is required for a broad distribution around a single center. These results are summarized in Table II.

In the Raman spectra for the FeNC series, the ratio of the D-band to G-band intensities ( $I_D/I_G$ ) was estimated to be 1.82 for FeNC-1, 1.35 for FeNC-2 and 1.38 for FeNC-3, suggesting that the addition of zinc into the precursor facilitated graphitization of the samples.

The electrocatalytic activity towards ORR was then quantitatively assessed by electrochemical measurements. From the RRDE voltammograms in Figure 7(a), apparent ORR activity can be seen for all samples, but the activity varies among the series. For instance, for FeNC-1, the onset potential ( $E_{\text{onset}}$ ) was identified at +0.813 V versus RHE and the limiting current at  $1.5 \text{ mA} \cdot \text{cm}^{-2}$ ; for FeNC-2, it is +0.993 V versus RHE and  $1.3 \text{ mA} \cdot \text{cm}^{-2}$ , and +0.704 V versus RHE and  $0.91 \text{ mA} \cdot \text{cm}^{-2}$  for FeNC-3. One can see that FeNC-2 emerged as the best among the samples, featuring an onset potential similar to that of Pt/C (+0.993 V). In the corresponding Tafel plots (Fig. 7(b)), the slopes are estimated to be  $-59.0 \text{ mV} \cdot \text{dec}^{-1}$ ,  $-61.4 \text{ mV} \cdot \text{dec}^{-1}$ ,  $-39.9 \text{ mV} \cdot \text{dec}^{-1}$ , and  $-4.9 \text{ mV} \cdot \text{dec}^{-1}$  for FeNC-1, FeNC-2, FeNC-3, and Pt/C 20%, respectively. One can see that the kinetic currents of all samples increased with an increase of the over potential, and FeNC-2 showed the highest kinetic current

**Table II.** Summary of the analysis of BET results.

Sample	DFT method			MP BET
	Pore volume ( $\text{cm}^3 \cdot \text{g}^{-1}$ )	Surface area ( $\text{m}^2 \cdot \text{g}^{-1}$ )	Half pore width (nm)	Surface area ( $\text{m}^2 \cdot \text{g}^{-1}$ )
FeNC-1	0.242	189.2	1.69	176.2
FeNC-2	1.267	745.6	2.38	914.3
FeNC-3	0.773	607.7	1.97	682.7

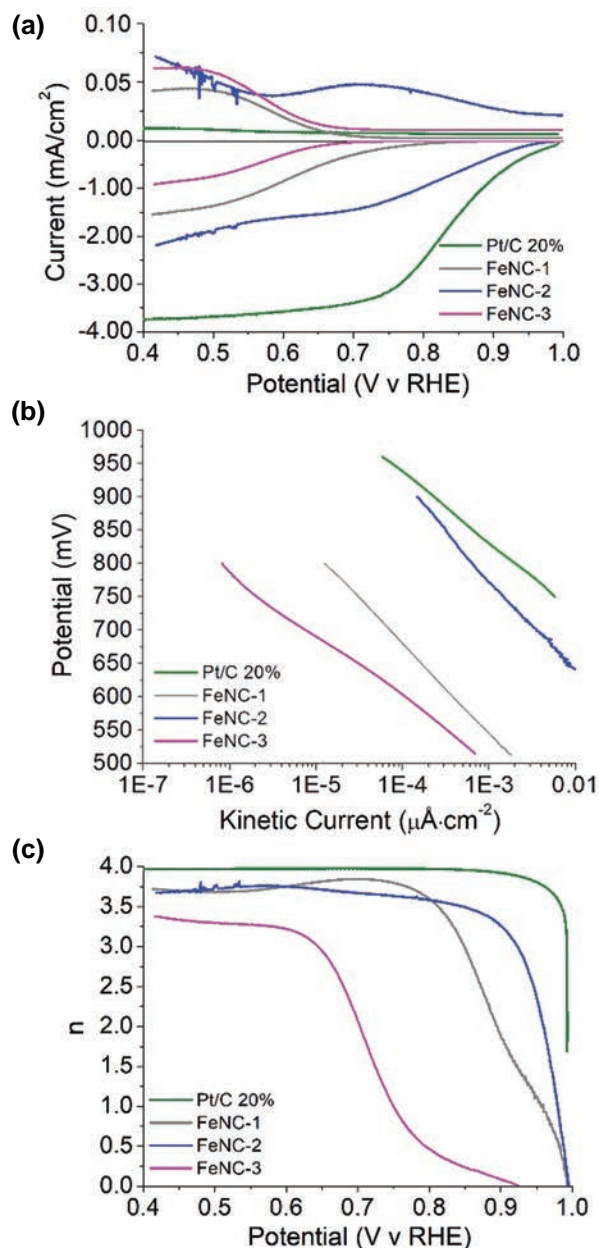


**Fig. 7.** (a) RRDE polarization curves of FeNC nanocomposites at the rotation rate of 2500 RPM and potential sweep rate of  $10 \text{ mV} \cdot \text{s}^{-1}$  in oxygen saturated 0.1 M KOH. Top: Ring current density. Bottom: Disk current density. (b) Tafel plot of FeNC catalysts. (c) Plot of the number of electrons transferred ( $n$ ) versus electrode potential.

in the potential range of +0.45 to +0.90 V. For instance, the kinetic current density at +0.80 V was  $12.5 \mu\text{A} \cdot \text{cm}^{-2}$ ,  $640 \mu\text{A} \cdot \text{cm}^{-2}$  and  $0.819 \mu\text{A} \cdot \text{cm}^{-2}$  for FeNC-1, FeNC-2, and FeNC-3, respectively. This, again, confirms that the FeNC-2 sample was the best catalyst in the FeNC series. Consistent behaviors were observed in the analysis of the electron-transfer number ( $n$ ) involved in ORR,  $n = 4I_{\text{Disk}} / (I_{\text{Disk}} + I_{\text{Ring}}/N)$ , where  $N$  is the collection efficiency (37%), and  $I_{\text{Disk}}$  and  $I_{\text{Ring}}$  are the disk and ring currents, respectively. These results are listed in

Figure 7(c). All FeNC samples showed an  $n$  number of at least 3.3, indicating that oxygen was mostly reduced to  $\text{OH}^-$  through the four-electron pathway.

The impact of pyrolysis temperature on the FeMOF- $\text{NH}_2$ -2 derived catalyst was also explored by pyrolyzing the FeMOF- $\text{NH}_2$ -2 precursor at 700 and 800 °C, labeled as FeNC-2-700 and FeNC-2-800, respectively (Fig. 8). One can see that FeNC-2-700 and FeNC-2-800 have an onset potential of +0.785 V versus RHE, almost 0.2 V more negative than that of FeNC-2 (prepared at 900 °C). In addition, FeNC-2-700 and FeNC-2-800 showed a limiting current density of  $1.1 \text{ mA} \cdot \text{cm}^{-2}$  and  $1.4 \text{ mA} \cdot \text{cm}^{-2}$  and kinetic current density of  $7.60 \mu\text{A} \cdot \text{cm}^{-2}$  and  $5.20 \mu\text{A} \cdot \text{cm}^{-2}$ , respectively, also markedly lower than that of FeNC-2. The lack of improvement in activity with the decrease in pyrolysis temperature illustrates the necessity of high temperature in pyrolytic preparation of the nanocomposites. FeNC-2 was also etched with 12 M hydrochloric acid overnight to examine the ORR activity without any surface particles. The onset potential of FeNC-2 worsened after etching with acid, indicating the importance of surface nanoparticles in the electrocatalysis of oxygen reduction.

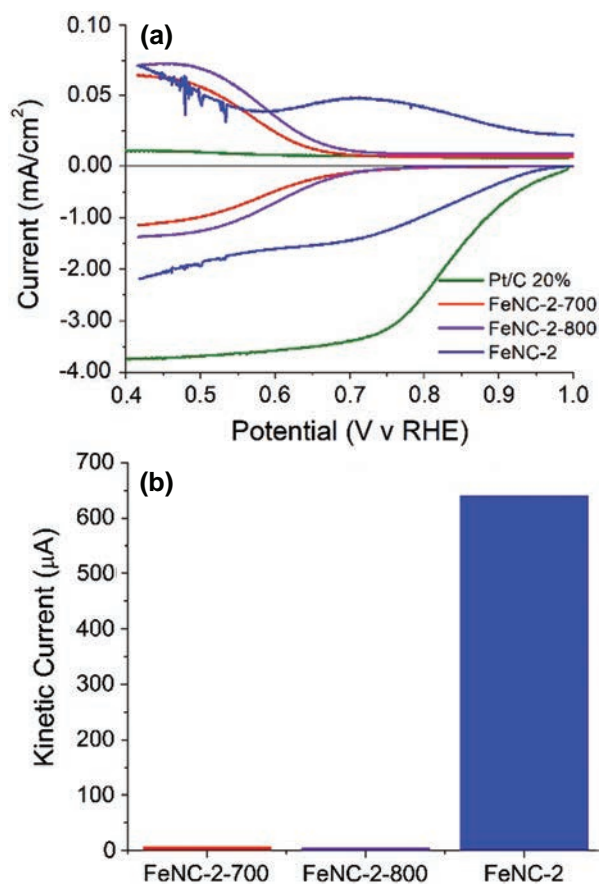


**Fig. 8.** (a) RRDE voltammograms of FeNC-2 prepared by pyrolysis of FeMOF- $\text{NH}_2$ -2 at varying temperatures at a rotation rate of 2500 RPM and potential sweep rate of  $10 \text{ mV} \cdot \text{s}^{-1}$  in oxygen saturated 0.1 M KOH. Top: Ring current density. Bottom: Disk current density. (b) Column plot comparing the kinetic current for each sample at +0.8 V.

In deriving porous nitrogen doped carbon catalysts from FeMOF-NH<sub>2</sub>-2, a nanocarbon structure with accessible surface iron carbide nanoparticles with high ORR activity is formed. The inclusion of zinc in the MOF has a positive effect on the final catalysts attained through pyrolysis. Increasing the amount of zinc in the precursory MOF has noticeable benefits on the design of the carbon catalyst up to FeMOF-NH<sub>2</sub>-2. The pore width increased from 3.384 nm to 4.764 nm, as did the surface area (189.2 m<sup>2</sup> · g<sup>-1</sup> to 745.6 m<sup>2</sup> · g<sup>-1</sup>) and pore volume (0.242 cm<sup>3</sup> · g<sup>-1</sup> to 1.267 cm<sup>3</sup> · g<sup>-1</sup>), making the surface more accessible. Of the FeNC catalysts, FeNC-2 has the highest activity, in coincidence with the highest concentration of Fe–C, highlighting the importance of the surface structural engineering in improving the catalytic activity. In addition, there is a positive correlation between the variables of pore structure (pore volume, pore width, and surface area), most probably because the increase in pore volume and pore width results in increased exposure of active sites. Without this activation, the surface is highly microporous and unsuitable for mass transfer and renders surface active sites less accessible to the reaction despite the higher concentration of iron species. Instead, FeNC-2 has a wide distribution of mesopores with a mean of 2.33 nm and mode of 2.38 nm which is conducive to mass transfer in ORR. When excess zinc was incorporated into FeMOF-NH<sub>2</sub>, the evaporation of zinc chloride during pyrolysis became increasingly destructive, decreasing the surface area and changing the nature of the pores. This prevented the formation of abundant mesopores with a mode of 2.38 nm and resulted in a trimodal distribution and lower mode pore width of 1.97 nm, leading to dampened activity. Taken together, these observations indicate that the maximal ORR activity of FeNC-2 among the series is likely the combined consequence of high Fe–C bonding moieties and optimal porosity.

Notably, in comparison to relevant porous Fe,N-codoped C catalysts reported in the literature,<sup>1, 23, 24, 27, 31, 35, 44, 47</sup> the onset potential of FeNC-2 (+0.997 V vs. RHE) is either more positive or comparable to the literature results. In addition, FeNC-2 has a larger surface area (745.62 m<sup>2</sup> · g<sup>-1</sup>) than several reported porous Fe<sub>3</sub>C/C catalysts.<sup>36, 37, 42, 46, 48</sup> Pore size distribution is also important. The generally smaller mesopores (2.38 nm) of FeNC-2 are advantageous in ORR electrocatalysis, in conjunction with the larger pore volume.

#### 4. SUMMARY

In this study, a series of mesoporous iron carbide@graphitic nanoparticles were derived by controlled pyrolysis of FeMOF-NH<sub>2</sub> at different zinc feeding ratios in the MIL-53-NH<sub>2</sub> synthesis. The pyrolysis was shown to not only graphitize the MOF and form Fe<sub>3</sub>C particles, but to evaporate the zinc compound to form pores whose nature were dependent on the feed ratio. Through BET

analysis, the optimal catalyst (FeNC-2) was shown to lack micropores and possess a distribution of small mesopores centered on 2.33 nm with a mode of 2.38 nm resulting in an ORR activity that is better than or comparable to other Fe–N–C catalysts in the literature. The impact of this simple yet crucial synthetic parameter presents an opportunity for further surface engineering of nanocarbon catalysts through the tuning of inorganic precursors.

**Acknowledgments:** The authors thank the National Science Foundation for partial support of the work (CHE-1710408 and CHE-1900235). This work was also supported by a Special Research Grant from the UCSC Committee on Research. TEM and XPS studies were performed at the National Center for Electron Microscopy and Molecular Foundry, Lawrence Berkeley National Laboratory, which is supported by the US Department of Energy, as part of a user project.

#### References and Notes

1. A. Aijaz, J. Masa, C. Rösler, H. Antoni, R. A. Fischer, W. Schuhmann, and M. Muhler, MOF-templated assembly approach for Fe<sub>3</sub>C nanoparticles encapsulated in bamboo-like N-doped CNTs: Highly efficient oxygen reduction under both acidic and basic conditions. *Chem. Eur. J.* 23, 12125 (2017).
2. O. Akhavan, The effect of heat treatment on formation of graphene thin films from graphene oxide nanosheets. *Carbon* 48, 509 (2010).
3. H. Ali, S. Zaman, I. Majeed, F. K. Kanodarwala, M. A. Nadeem, J. A. Stride, and M. A. Nadeem, Porous carbon/rGO composite: An ideal support material of highly efficient palladium electrocatalysts for the formic acid oxidation reaction. *Chemelectrochem* 4, 3126 (2017).
4. S. Bauer, C. Serre, T. Devic, P. Horcajada, J. Marrot, G. Férey, and N. Stock, High-throughput assisted rationalization of the formation of metal organic frameworks in the iron (III) aminoterephthalate solvothermal system. *Inorg. Chem.* 47, 7568 (2008).
5. A. K. Bhattacharya, D. R. Pyke, G. S. Walker, and C. R. Werrett, The surface reactivity of different aluminas as revealed by their XPS Cls spectra. *Appl. Surf. Sci.* 108, 465 (1997).
6. L. M. Chen, P. G. Hu, C. P. Deming, N. Wang, J. E. Lu, and S. W. Chen, Intervalence charge transfer of ruthenium–nitrogen moieties embedded within nitrogen-doped graphene quantum dots. *J. Phys. Chem. C* 120, 13303 (2016).
7. M. Chen, Y. Jiang, P. Mei, Y. Zhang, X. F. Zheng, W. Xiao, Q. L. You, X. M. Yan, and H. L. Tang, Polyacrylamide microspheres-derived Fe<sub>3</sub>C@N-doped carbon nanospheres as efficient catalyst for oxygen reduction reaction. *Polymers* 11, 767 (2019a).
8. P. Chen, L.-K. Wang, G. Wang, M.-R. Gao, J. Ge, W.-J. Yuan, Y.-H. Shen, A.-J. Xie, and S.-H. Yu, Nitrogen-doped nanoporous carbon nanosheets derived from plant biomass: An efficient catalyst for oxygen reduction reaction. *Energy Environ. Sci.* 7, 4095 (2014).
9. X. Chen, J. Y. Xu, H. Chai, Y. C. Wang, D. Z. Jia, and W. Y. Zhou, One-step synthesis of hollow chain-like nitrogen doped carbon nanotubes/iron carbide as highly efficient bifunctional oxygen electrocatalyst. *J. Electroanal. Chem.* 838, 16 (2019b).
10. M. Ferrandon, A. J. Kropf, D. J. Myers, K. Artyushkova, U. Kramm, P. Bogdanoff, G. Wu, C. M. Johnston, and P. Zelenay, Multitechnique characterization of a polyaniline–iron–carbon oxygen reduction catalyst. *J. Phys. Chem. C* 116, 16001 (2012).
11. A. Furlan, U. Jansson, J. Lu, L. Hultman, and M. Magnusson, Structure and bonding in amorphous iron carbide thin films. *J. Phys.-Condens. Matter* 27, 045002 (2015).



12. J. Gautam, T. D. Thanh, K. Maiti, N. H. Kim, and J. H. Lee, Highly efficient electrocatalyst of N-doped graphene-encapsulated cobalt-iron carbides towards oxygen reduction reaction. *Carbon* 137, 358 (2018).
13. C. Haavik, S. Stolen, H. Fjellvag, M. Hanfland, and D. Hausermann, Equation of state of magnetite and its high-pressure modification: Thermodynamics of the Fe–O system at high pressure. *Am. Min.* 85, 514 (2000).
14. F. Hao, Y. Yao, Y. P. Li, C. X. Tian, X. H. Zhang, and J. H. Chen, Synthesis of high-concentration B and N co-doped porous carbon polyhedra and their supercapacitive properties. *RSC Adv.* 5, 77527 (2015).
15. P. G. Hu, K. Liu, C. P. Deming, and S. W. Chen, Multifunctional graphene-based nanostructures for efficient electrocatalytic reduction of oxygen. *J. Chem. Technol. Biotechnol.* 90, 2132 (2015).
16. Y. Hu, J. O. Jensen, W. Zhang, L. N. Cleemann, W. Xing, N. J. Bjerrum, and Q. F. Li, Hollow spheres of iron carbide nanoparticles encased in graphitic layers as oxygen reduction catalysts. *Angew. Chem.-Int. Edit.* 53, 3675 (2014).
17. M. Lefevre, E. Proietti, F. Jaouen, and J. P. Dodelet, Iron-based catalysts with improved oxygen reduction activity in polymer electrolyte fuel cells. *Science* 324, 71 (2009).
18. L. J. Li, J. X. He, Y. Wang, X. X. Lv, X. Gu, P. C. Dai, D. D. Liu, and X. B. Zhao, Metal-organic frameworks: A promising platform for constructing non-noble electrocatalysts for the oxygen-reduction reaction. *J. Mater. Chem. A* 7, 1964 (2019).
19. L. Lin, Q. Zhu, and A. W. Xu, Noble-metal-free Fe–N/C catalyst for highly efficient oxygen reduction reaction under both alkaline and acidic conditions. *J. Am. Chem. Soc.* 136, 11027 (2014).
20. Y. X. Liu, T. F. Li, X. Y. Cao, J. J. Liu, J. Zhang, J. Jia, F. Wang, and K. Pan, Electrospun Fe<sub>2</sub>C-loaded carbon nanofibers as efficient electrocatalysts for oxygen reduction reaction. *Nanotechnology* 30, 325403 (2019).
21. B. Z. Lu, L. Guo, F. Wu, Y. Peng, J. E. Lu, T. J. Smart, N. Wang, Y. Z. Finfrock, D. Morris, P. Zhang, N. Li, P. Gao, Y. Ping, and S. W. Chen, Ruthenium atomically dispersed in carbon outperforms platinum toward hydrogen evolution in alkaline media. *Nat. Commun.* 10, 631 (2019).
22. B. Z. Lu, T. J. Smart, D. D. Qin, J. E. Lu, N. Wang, L. M. Chen, Y. Peng, Y. Ping, and S. W. Chen, Nitrogen and iron-codoped carbon hollow nanotubes as high-performance catalysts toward oxygen reduction reaction: A combined experimental and theoretical study. *Chem. Mater.* 29, 5617 (2017).
23. Y. Luo, J. Zhang, Y. H. Chen, Z. J. Li, J. W. Chen, G. Wang, and R. L. Wang, MOF-derived porous carbon supported iron-based catalysts with optimized active sites towards oxygen reduction reaction. *J. Electroanal. Chem.* 847, 113191 (2019).
24. Y. Luo, J. Zhang, M. Kiani, Y. H. Chen, J. W. Chen, G. Wang, S. H. Chan, and R. L. Wang, Synthesis of MOF-derived nonprecious catalyst with high electrocatalytic activity for oxygen reduction reaction. *Ind. Eng. Chem. Res.* 57, 12087 (2018).
25. S. Q. Ma, G. A. Goenaga, A. V. Call, and D. J. Liu, Cobalt imidazole framework as precursor for oxygen reduction reaction electrocatalysts. *Chem. Eur. J.* 17, 2063 (2011).
26. K. I. Ozoemena, Nanostructured platinum-free electrocatalysts in alkaline direct alcohol fuel cells: Catalyst design, principles and applications. *RSC Adv.* 6, 89523 (2016).
27. J. Park, H. Lee, Y. E. Bae, K. C. Park, H. Ji, N. C. Jeong, M. H. Lee, O. J. Kwon, and C. Y. Lee, Dual-functional electrocatalyst derived from iron-porphyrin encapsulated metal-organic frameworks. *ACS Appl. Mater. Interfaces* 9, 28758 (2017).
28. Y. Peng and S. W. Chen, Electrocatalysts based on metal@carbon core@shell nanocomposites: An overview. *Green Energy Environ.* 3, 335 (2018).
29. Y. Peng, B. Z. Lu, and S. W. Chen, Carbon-supported single atom catalysts for electrochemical energy conversion and storage. *Adv. Mater.* 30, 1801995 (2018).
30. K. S. W. Sing, D. H. Everett, R. A. W. Haul, L. Moscou, R. A. Pierotti, J. Rouquerol, and T. Siemieniowska, Reporting Physisorption data for gas solid systems with special reference to the determination of surface-area and porosity (recommendations 1984). *Pure Appl. Chem.* 57, 603 (1985).
31. C. S. Song, S. K. Wu, X. P. Shen, X. L. Miao, Z. Y. Ji, A. H. Yuan, K. Q. Xu, M. M. Liu, X. L. Xie, L. R. Kong, G. X. Zhu, and S. A. Shah, Metal-organic framework derived Fe/Fe<sub>3</sub>C@N-doped-carbon porous hierarchical polyhedrons as bifunctional electrocatalysts for hydrogen evolution and oxygen-reduction reactions. *J. Colloid Interface Sci.* 524, 93 (2018).
32. H. B. Tan, Y. Q. Li, J. Kim, T. Takei, Z. L. Wang, X. T. Xu, J. Wang, Y. Bando, Y. M. Kang, J. Tang, and Y. Yamauchi, Sub-50 nm iron-nitrogen-doped hollow carbon sphere-encapsulated iron carbide nanoparticles as efficient oxygen reduction catalysts. *Adv. Sci.* 5, 1800120 (2018).
33. H. B. Tan, J. Tang, J. Kim, Y. V. Kaneti, Y. M. Kang, Y. Sugahara, and Y. Yamauchi, Rational design and construction of nanoporous iron- and nitrogen-doped carbon electrocatalysts for oxygen reduction reaction. *J. Mater. Chem. A* 7, 1380 (2019).
34. J. F. Tu, N. Rajule, Y. Liu, and J. Martin, Nanostructure diffraction analysis of a copper/single walled carbon nanotube nanocomposite synthesized by laser surface implanting. *Carbon* 113, 1 (2017).
35. H. Wang, F. X. Yin, N. Liu, R. H. Kou, X. B. He, C. J. Sun, B. H. Chen, D. J. Liu, and H. Q. Yin, Engineering Fe–Fe<sub>3</sub>C@Fe–N–C active sites and hybrid structures from dual metal-organic frameworks for oxygen reduction reaction in H-2-O-2 fuel cell and Li-O-2 battery. *Adv. Funct. Mater.* 29, 1901531 (2019a).
36. S. H. Wang, X. Yan, K. H. Wu, X. M. Chen, J. M. Feng, P. Y. Lu, H. Feng, H. M. Cheng, J. Liang, and S. X. Dou, A hierarchical porous Fe–N impregnated carbon-graphene hybrid for high-performance oxygen reduction reaction. *Carbon* 144, 798 (2019b).
37. X. J. Wang, H. G. Zhang, H. H. Lin, S. Gupta, C. Wang, Z. X. Tao, H. Fu, T. Wang, J. Zheng, G. Wu, and X. G. Li, Directly converting Fe-doped metal organic frameworks into highly active and stable Fe–N–C catalysts for oxygen reduction in acid. *Nano Energy* 25, 110 (2016).
38. Y. Wang, J. Li, and Z. D. Wei, Recent progress of carbon-based materials in oxygen reduction reaction catalysis. *ChemElectroChem* 5, 1764 (2018).
39. I. G. Wood, L. Voadlo, K. S. Knight, D. P. Dobson, W. G. Marshall, G. D. Price, and J. Brodholt, Thermal expansion and crystal structure of cementite, Fe(3)C, between 4 and 600 K determined by time-of-flight neutron powder diffraction. *J. Appl. Crystallogr.* 37, 82 (2004).
40. Z. Y. Wu, X. X. Xu, B. C. Hu, H. W. Liang, Y. Lin, L. F. Chen, and S. H. Yu, Iron carbide nanoparticles encapsulated in mesoporous Fe–N-doped carbon nanofibers for efficient electrocatalysis. *Angew. Chem.-Int. Edit.* 54, 8179 (2015).
41. M. L. Xiao, J. B. Zhu, L. G. Feng, C. P. Liu, and W. Xing, Meso/macroporous nitrogen-doped carbon architectures with iron carbide encapsulated in graphitic layers as an efficient and robust catalyst for the oxygen reduction reaction in both acidic and alkaline solutions. *Adv. Mater.* 27, 2521 (2015).
42. M. L. Xiao, J. B. Zhu, L. Ma, Z. Jin, J. Ge, X. J. Deng, Y. Hou, Q. G. He, J. K. Li, Q. Y. Jia, S. Mukerjee, R. Yang, Z. Jiang, D. S. Su, C. P. Liu, and W. Xing, Microporous framework induced synthesis of single-atom dispersed Fe–N–C acidic ORR catalyst and its in situ reduced Fe–N-4 active site identification revealed by X-ray absorption spectroscopy. *ACS Catal.* 8, 2824 (2018).
43. T. Yamashita and P. Hayes, Analysis of XPS spectra of Fe<sup>2+</sup> and Fe<sup>3+</sup> ions in oxide materials. *Appl. Surf. Sci.* 254, 2441 (2008).
44. L. M. Yang, Y. Z. Bai, H. J. Zhang, J. T. Geng, Z. G. Shao, and B. L. Yi, Nitrogen-doped porous carbon derived from Fe-MIL nanocrystals as an electrocatalyst for efficient oxygen reduction. *RSC Adv.* 7, 22610 (2017).
45. X. R. Zhang, Y. B. Mollamahale, D. D. Lyu, L. Z. Liang, F. Yu, M. Qing, Y. H. Du, X. Y. Zhang, Z. Q. Tian, and P. K. Shen,

- Molecular-level design of Fe–N–C catalysts derived from Fe-dual pyridine coordination complexes for highly efficient oxygen reduction. *J. Catal.* 372, 245 (2019).
46. Z. P. Zhang, J. T. Sun, F. Wang, and L. M. Dai, Efficient oxygen reduction reaction (ORR) catalysts based on single iron atoms dispersed on a hierarchically structured porous carbon framework. *Angew. Chem.-Int. Edit.* 57, 9038 (2018).
47. P. P. Zhao, X. Hua, W. Xu, W. Luo, S. L. Chen, and G. Z. Cheng, Metal-organic framework-derived hybrid of Fe<sub>3</sub>C nanorod-encapsulated, N-doped CNTs on porous carbon sheets for highly efficient oxygen reduction and water oxidation. *Catal. Sci. Technol.* 6, 6365 (2016).
48. R. Zhao, W. Xia, C. Lin, J. L. Sun, A. Mahmood, Q. F. Wang, B. Qiu, H. Tabassum, and R. Q. Zou, A pore-expansion strategy to synthesize hierarchically porous carbon derived from metal-organic framework for enhanced oxygen reduction. *Carbon* 114, 284 (2017).
49. S. L. Zhao, H. J. Yin, L. Du, L. C. He, K. Zhao, L. Chang, G. P. Yin, H. J. Zhao, S. Q. Liu, and Z. Y. Tang, Carbonized nanoscale metal-organic frameworks as high performance electrocatalyst for oxygen reduction reaction. *ACS Nano* 8, 12660 (2014).